JACS
JOURNAL OF THE AMERICAN CHEMICAL SOCIETY
Article
pubs.acs.org/JACS

# Theoretical Prediction and Experimental Confirmation of Unusual Ternary Ordered Semiconductor Compounds in Sr−Pb−S System

Shiqiang Hao,[†] Li-Dong Zhao,[‡,§] Chang-Qiang Chen,[†,§] Vinayak P. Dravid,[†] Mercouri G. Kanatzidis,[‡] and Christopher M. Wolverton*[,†]

[†]Department of Materials Science & Engineering, and [‡]Department of Chemistry, Northwestern University, Evanston, Illinois 60208, United States

Supporting Information

**ABSTRACT:** We examine the thermodynamics of phase separation and ordering in the ternary $Ca_xPb_{1-x}S$ and $Sr_xPb_{1-x}S$ systems by density-functional theory combined with a cluster expansion and Monte Carlo simulations. Similar to most other ternary III−V or IV−VI semiconductor alloys, we find that bulk phase separation is thermodynamically preferred for PbS−CaS. However, we predict the surprising existence of stable, ordered ternary compounds in the PbS−SrS system. These phases are previously unreported ordered rocksalt-based compounds: $SrPb_3S_4$, $SrPbS_2$, and $Sr_3PbS_4$. The stability of these predicted ordered phases is confirmed by transmission electron microscopy observations and band gap measurements. We believe this work paves the way for a combined theory-experiment approach to decipher complex phase relations in multicomponent chalcogenide systems.

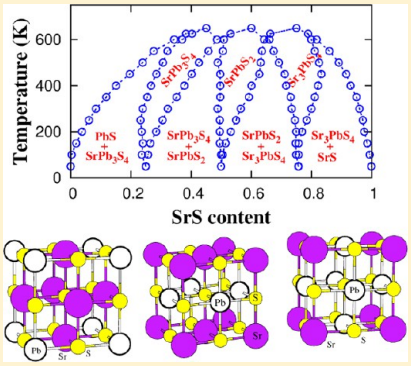


## 1. INTRODUCTION

For many semiconductor applications, a traditional way to tune material properties is through the formation of intermediate ternary alloys $A_{1-x}B_xC$ from combinations of isostructural binary semiconductor compounds AC and BC.[1] These intermediate alloys may consist of random, ordered, or phase-separated substitution of constituent elements on the lattice sites of the parent crystal structure. This order/disorder in such atomic-scale structures decides much of the electronic, optical, and transport properties of the alloy systems. For example, the optical band gap, transport effective mass, and thermal transport of ordered alloys are significantly different from those of random alloys at the same chemical composition.[1] However, a long-standing paradigm in this field suggests that the formation enthalpy of (random or ordered) intermediate ternary semiconductor alloys is often unfavorable relative to phase separation into the pure binary compounds because of the strain energy penalty induced by lattice mismatch.[2,3] Consequently, the thermodynamics of these alloys are typically characterized by miscibility gaps in the composition/temperature phase diagrams containing phase separation between two phases (one A-rich and the other B-rich) at their own equilibrium lattice constants. For example, the phase diagrams of commonly used semiconductors of II−VI, III−V, and IV−VI (such as Zn(O,S),[4,5] (Ga,In)N,[6,7] Ga(P,Sb),[7] Pb(S,Se),[8] (Pb,Sn)Te,[8] etc.) all exhibit bulk incoherent phase separation. To enhance solid solubility or form ordered phases in these $A_{1-x}B_xC$ systems, epitaxial growth techniques[2] can be employed to reduce strain energy[9] or provide a barrier to incoherent phase separation, and hence induce long-range ordering. Yet all of these phenomena have led to the widely held view that the microscopic interactions between the local bonding configurations in such alloys are fundamentally repulsive, and hence no long-range-ordered intermediate isovalent compounds are to be expected in bulk semiconductor physics.

Lead chalcogenide compounds have been studied extensively as high thermoelectric efficiency materials. Alloying lead chalcogenides with a small amount of other semiconductor compounds can increase the figure of merit through the formation of nanoprecipitates, which reduce the lattice thermal conductivity without significantly compromising the electronic conductivity.[10−13] In this Article, we focus on the phase stability of CaS and SrS as the second phase candidates to the host material PbS. We have previously shown that small fractions of added nanoprecipitates in PbS can raise its figure of merit *ZT* from 0.4 to 1.2 at 900 K.[10,11] Both CaS and SrS possess the simple rocksalt structure (as does PbS) but with different lattice mismatch with PbS, and no experimental ternary phase diagrams of PbS−CaS or PbS−SrS are currently available. We report an exhaustive first-principles study of the atomic structure and thermodynamics of ordering and phase stability in the ternary $Ca_xPb_{1-x}S$ and $Sr_xPb_{1-x}S$ systems using density functional theory (DFT) and cluster expansion (CE) calculations. The calculated composition−temperature phase diagram for the incoherent $Ca_xPb_{1-x}S$ system indicates the existence of a miscibility gap, qualitatively similar to all other III−V and IV−VI ternary alloy systems. Interestingly, however, the calculated phase diagram of $Sr_xPb_{1-x}S$ predicts a very different behavior, stable ordered compound formation at 25%,

**Received:** November 27, 2013
**Published:** January 7, 2014

  

50%, and 75% compositions of SrS. To our knowledge, these new $Sr_3PbS_4$, $SrPbS_2$, and $SrPb_3S_4$ compounds have not been hitherto reported, and hence represent a true computational prediction of our DFT and CE methodology. More importantly, we confirm the existence of the ordered phases $SrPbS_2$ and $SrPb_3S_4$ by successful experimental synthesis and validation using transmission electron microscopy and band gap measurements. Even though much work can predict new phases that were not previously known to be stable with computations,[14−18] the true predictions verified by experimental observations are still relatively uncommon.[17,19] Band structure calculations show that these highly symmetric ordered phases have direct band gaps in a range of 0.3−4.2 eV, and hence could be relevant for a variety of semiconductor technologies. This discovery of ordered compounds suggests that alloying lead chalcogenides with large amounts of other compounds is a possible strategy to search for new semiconductors with tuned band structures for practical applications.

## 2. COMPUTATIONAL AND EXPERIMENTAL METHODOLOGIES

**Calculations.** The total energies and relaxed geometries were calculated by the density-functional theory within the generalized gradient approximation,[20,21] with periodic boundary conditions and a plane wave basis set as implemented in the Vienna ab initio simulation package.[22] The formation energy $\Delta H$ of a $A_{1-x}B_xC$ with respect to the energies of constituents AC and BC is defined as $\Delta H(\sigma) = E_{tot}(\sigma) - (1 - x)E_{tot}^{AC} - xE_{tot}^{BC}$, where $E_{tot}(\sigma)$, $E_{tot}^{AC}$, and $E_{tot}^{BC}$ are total energies of phases $A_{1-x}B_xC$, AC, and BC, respectively. The formation energies were numerically converged to approximately 1 meV/cation using a basis set energy cutoff of 300 eV and dense $k$-meshes corresponding to 2000 per reciprocal atom $k$-points in the Brillouin zone. Test calculations using different LDA, GGA(PW91), and GGA(PBE) functionals have shown that the formation energies differ only slightly (around 0.0008 eV/cation). All exchange correlations give negative formation energies for PbS/SrS, demonstrating that the prediction of stable ordered compounds is independent of functional. The Gibbs free energies are calculated by $\Delta G = \Delta H - T\Delta S$, where $\Delta H$ is the formation energy as mentioned above. For the PbS/CaS system, the mixing entropy $\Delta S$ is calculated by the subregular solution model. On the basis of this model, the phase diagram of PbS/CaS is shown as a red line in Figure 1c. For the ordered case PbS/SrS, the vibrational entropies $\Delta S$ are also calculated. To calculate the band gap for a given unit cell, the energy eigenvalues at each $k$-point in the Brillouin zone are evaluated, and the band gap values are determined from the difference between the conduction-band minimum (minimum energy unoccupied state) and valence-band maximum (maximum energy occupied state). The cluster expansion approach[23] was used to construct an effective Hamiltonian for energy evaluation on the rocksalt-based $Ca_xPb_{1-x}S$ and $Sr_xPb_{1-x}S$ structures. We used the ATAT toolkit[24] to obtain the optimal effective cluster interactions from fully relaxed total energies of ordered input structures. By fitting 24 ordered input structures, the final cluster expansion for PbS/CaS (PbS/SrS) uses 10(21) interaction coefficients, including 3(7) pairs, 2(12) three-body, and 3(0) four-body interactions, resulting in a leave-one-out cross-validation score as good as 5.5(5.3) meV/cation. The detailed clusters and effective cluster interactions are listed in Table S1 in the Supporting Information.

On the basis of the well-converged effective cluster interactions, the temperature−composition phase diagrams are calculated by semi-Grand Canonical Monte Carlo (GCMC) simulations.[25] In this semigrand canonical ensemble, the energy and concentration of an alloy (with a fixed total number of atoms) are allowed to fluctuate, while temperature and chemical potentials are externally imposed. By scanning over temperature and chemical potentials, the two-phase regions in the phase diagram can be determined from discontinuities

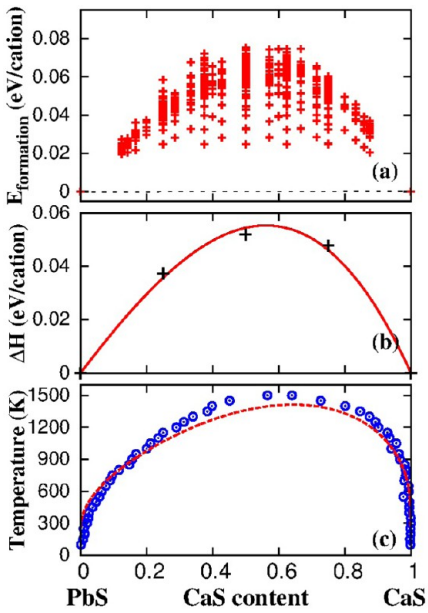


**Figure 1.** Calculated energies and phase diagram of PbS−CaS. Formation energies from CE (a), mixing energies of solid solution (fit to a subregular solution model) (b), and incoherent miscibility gap (c) of the PbS−CaS system. In (a), the symbols indicate energies predicted by cluster expansion for possible ordered structures, and the ground-state convex hull contains only PbS and CaS with no stable intermediate compounds. In (b), the DFT-calculated formation energies of three SQS are shown as "+". The blue "O" and red dashed line in (c) are calculated separately by GCMC and subregular solution model.

of composition as a function of chemical potential. We use a 40 × 40 × 40 unit cell as a simulation cell, and the simulated temperatures range from 50 to 2000 K with a 50 K interval. We use 40 000 MC steps to equilibrate and 60 000 MC steps for averaging, and we monitor the composition change with chemical potential at a given temperature. The thermodynamic state is thus determined as a function of the temperature and the chemical potential differences of the constituents. To check for hysteresis in the phase diagram results, we have repeated Monte Carlo simulations by stepping through chemical potential in both directions. We find no big differences between these two simulations, confirming the accuracy of the phase diagrams.

**Synthesis.** Reagent chemicals were used as obtained: Pb wire (99.99%, American Elements, U.S.), S shot or chunk (99.999%, Inc., Canada), Sr chunk (99.9%, Cerac, U.S.), and Ca redistilled granule (99.5%, Alfa Aesar, U.S.). $Sr_xPb_{1-x}S$ and $Ca_xPb_{1-x}S$ ($x$ = 0, 0.10, 0.25, 0.50, 0.75, 0.90, and 1.0) samples were synthesized by a melting reaction using elemental Sr, Ca, Pb, and S inside carbon-coated fused quartz tubes (Ø ≈ 20 mm) in an $N_2$-filled glovebox. The tubes were then evacuated to a pressure of ~$10^{-4}$ Torr, flame-sealed, slowly heated to 723 K in 12 h, then to 1423 K in 7 h, soaked at this temperature for 6 h, and subsequently furnace cooled to room temperature. The obtained ingots were crushed into powders and then densified by spark plasma sintering (SPS) method (SPS-211Lx, Dr. Sinter). To prepare for SPS processing, the powders were densified at 923 K for 2 min in a 12.7 mm diameter graphite die under an axial compressive stress of 40 MPa.

**XRD Phase Analysis.** Samples pulverized with an agate mortar were used for powder X-ray diffraction. Powder X-ray diffraction patterns were collected at room temperature using a calibrated CPS 120 INEL powder X-ray diffractometer (Cu K$\alpha$, $\lambda$ = 1.5418 Å) operating at 40 kV/20 mA and equipped with a position-sensitive detector.

**Transmission Electron Microscopy (TEM).** TEM specimens were prepared following the standard procedure of grinding, dimpling, polishing, and ion milling. Extreme care was taken to avoid damaging


dx.doi.org/10.1021/ja411857y | J. Am. Chem. Soc. 2014, 136, 1628−1635

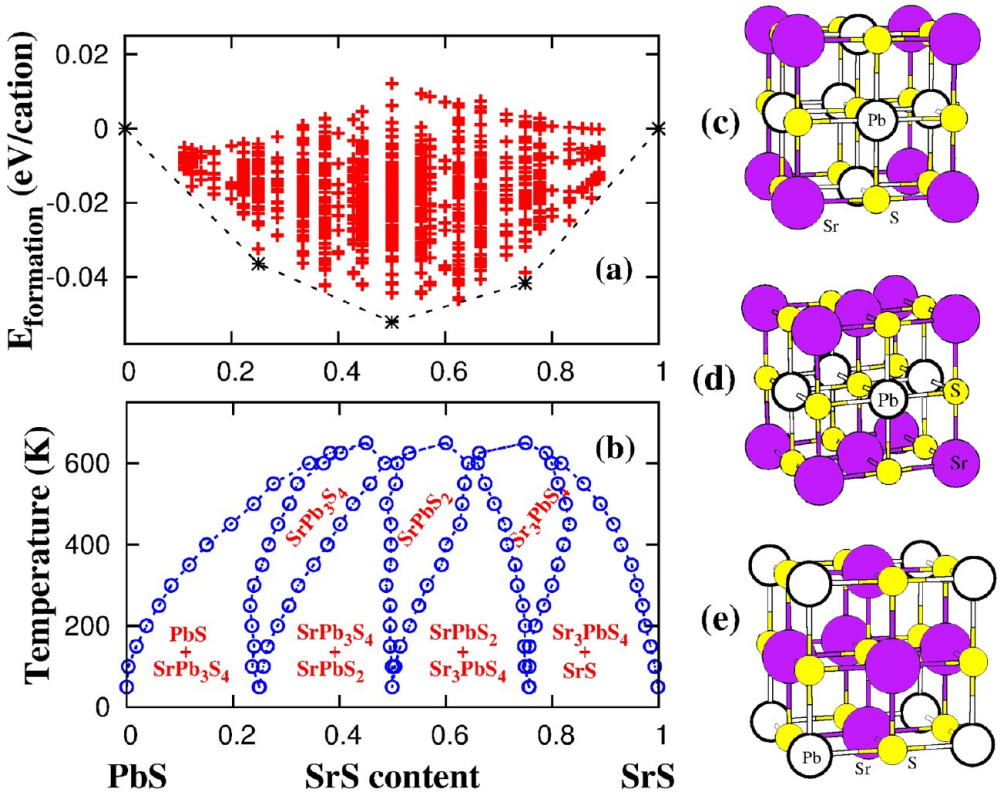


**Figure 2.** Formation energy (a) and temperature−composition phase diagram (b) of PbS and SrS mixing phases. Same as those in Figure.1, the "+" means the energies predicted by cluster expansion for possible structures, and the "*" indicates the energies of DFT calculated ground states. The ordered phases are $SrPb_3S_4$, $SrPbS_2$, and $Sr_3PbS_4$, corresponding to three ground states at 25%, 50%, and 75% in (a). The corresponding crystal structures are plotted in (c), (d), and (e), respectively.

the specimen by using a gentle mill using a low accelerating voltage of 2.8 kV at low incident angle (4°) and at cryogenic specimen temperature. The TEM specimens were examined in a JEOL 2100F transmission electron microscope operated at 200 kV.

**Band Gap Measurements.** Room-temperature optical diffuse reflectance measurements were performed on finely ground powders to probe optical energy gap of the series. The spectra were collected in the mid-IR range using a Nicolet 6700 FT-IR (Fourier transform infrared spectrometry) spectrometer to measure the samples with band gap less than 0.5 eV.[11] For the samples with expected band gaps larger than 0.5 eV, measurements were performed using a Shimadzu model UV-3101PC double-beam, double-monochromator spectrophotometer (ultraviolet−visible absorption spectroscopy).[26] $BaSO_4$ was used as a 100% reflectance standard. The generated reflectance versus wavelength data were used to estimate the band gap by converting reflectance to absorption data according to Kubelka−Munk equations: $\alpha/S = (1 - R)^2/(2R)$, where $R$ is the reflectance and $\alpha$ and $S$ are the absorption and scattering coefficients, respectively.[27]

## 3. RESULTS AND DISCUSSION

**3.1. Phase Stability in PbS−CaS.** Using the DFT+CE computational methodology, we predict the stable phases of $Ca_xPb_{1-x}S$ and the formation energy of all 16 076 rocksalt-based ordered structures with less than 18 atoms per unit cell shown in Figure 1a. By constructing the convex hull (the lowest-energy set of tie-lines such that no structure lies below the hull), we can identify the ground-state structures at 0 K as a function of composition. Figure 1a shows that the rocksalt-based PbS−CaS alloy system prefers phase separation because the formation energies of all compounds are positive, and hence unfavorable with respect to decomposition into pure PbS and CaS. Figure 1c shows the phase diagram of PbS−CaS as obtained from Monte Carlo simulations. The miscibility gap indicates regions of phase separation between PbS-rich and CaS-rich rocksalt solid solutions. There is a pronounced asymmetry in solubility. The CaS phase can accommodate very little solubility of PbS (only about 1% at 900 K); on the contrary, the solid-state solubility of CaS in the PbS phase can be as high as 6% at 600 K. We note that in our cluster expansion calculations, all alloy structures including phase-separated PbS and CaS constituents, ordered or disordered alloy structures, maintain their own lattice structures and lattice constants, giving up mutual coherence. There is no coherency strain between phases, and hence our calculated phase diagram is incoherent. Thus, the bulk thermodynamic equilibrium in the PbS−CaS phase diagram is an incoherent miscibility gap.

The incoherent miscibility gap between PbS and CaS obtained from CE and GCMC includes effects of short-range order in the solid solution and non-mean-field configurational entropy. A much simpler method to calculate incoherent phase stability is the subregular solution model.[8] By comparing our MC results with those from a subregular solution, we can quantify the effects of short-range order and non-mean-field entropy on the phase diagram. According to the subregular solution model, the incoherent mixing formation enthalpy can be expressed as a polynomial function of composition, which can be simply fitted by the mixing energies of three special quasirandom structures (SQSs)[28] at 25%, 50%, and 75% compositions. These SQSs are ordered structures with relatively small unit cell, with atoms placed on lattice sites in such a way as to mimic the pair and multibody correlations of a perfectly random lattice. SQSs allow one to treat random solid


dx.doi.org/10.1021/ja411857y | J. Am. Chem. Soc. 2014, 136, 1628−1635

solutions at the DFT level, including the important physical effects of local atomic relaxations, without the computational cost of configurationally averaging a large supercell. The DFT mixing energies of the 32 atom SQS cell and the subregular solution model fitted mixing energy curve are shown in Figure 1b. By adding the ideal (mean-field) mixing entropy to the mixing energies, we obtain the Gibbs free energy. The miscibility gap is determined from a straightforward common-tangent approach. The incoherent miscibility gap calculated by the subregular solution model is plotted in Figure 1c as a dashed line. The miscibility gaps from CE with GCMC and subregular solution model agree very well, indicating that non-mean-field configurational entropy and short-range order are minor effects in this system.

To experimentally verify our calculated results for PbS−CaS, we carried out the synthesis of mixtures corresponding to 50% CaS and 50% PbS, as described in the experimental section. XRD of the resulting mixture (Supporting Information Figure S1) shows that this nominal composition of $CaPbS_2$ is not a single phase, but rather is composed of PbS and CaS phases. Thus, the experimental results indicate that there is no solid solution or ordered compounds between 50% CaS and 50% PbS, entirely consistent with the calculations in Figure 1.

**3.2. Phase Stability in PbS−SrS.** We next describe similar calculations of mixing between PbS and SrS. Interestingly, the formation energies of PbS−SrS alloys are quite different from those of the PbS−CaS system. The formation energies of $Sr_xPb_{1-x}S$ are often negative, indicating the stability of the compounds relative to the pure end members PbS and SrS. Thus, in contrast to the phase-separating PbS−CaS system, we find the unexpected result that PbS−SrS is a compound-forming system. Using the DFT-derived cluster expansion, we determine the temperature−composition phase diagram of PbS−SrS by GCMC simulations [Figure 2b]. There are three predicted ordered phases in the phase diagram, corresponding to three $T$ = 0 K ground states with stoichiometries: $SrPb_3S_4$, $SrPbS_2$, and $Sr_3PbS_4$. We note, however, that at finite temperatures, each of these phases is stable for a range of off-stoichiometric compositions. Also, each phase undergoes an order−disorder transformation into a stable, disordered rocksalt solid solution at high temperature. There are also several regions of stable two-phase coexistence.

The three ground-state structures identified at 25%, 50%, and 75% SrS compositions are shown in Figure 2c−e. All three compounds are ordered superstructures of rocksalt, with Pb and Sr decorating the cation sublattice and S occupying the anion sublattice. For $SrPb_3S_4$, Pb and Sr atoms occupy the face center and corner positions of the rocksalt cation sublattice, respectively. The structure of $Sr_3PbS_4$ is related to that of $SrPb_3S_4$ by switching the relative positions of Pb and Sr. Both structures exhibit cubic symmetry. On the other hand, the $SrPbS_2$ structure is tetragonal and consists of alternatively stacked (100) cation layers of Pb and Sr. Interestingly, these orderings of cations on the fcc sublattice correspond to $L1_2$, $L1_0$, and $L1_2$ type structures, commonly found in intermetallic systems, such as the prototypical Cu−Au system.[29] However, to the best of our knowledge, the phase diagrams of PbS−SrS and our predicted new ordered phases have not been reported, and are quite unexpected, given the prevalence of phase-separation tendencies in semiconductor alloys.

Our cluster expansion and GCMC simulations explore the effects of configurational thermodynamics on phase stability. However, vibrational thermodynamics form another important contribution to phase stability.[30] The vibrational properties are also of interest for semiconductor thermoelectrics because of their impact on thermal conductivity, especially at elevated temperatures where thermoelectrics often operate. For example, recent studies on Cu−Sb−Se,[31] $NaSbTe_2$,[32] and ZrCoSb[33] ternary semiconductors have shown the role of DFT calculations of anharmonic vibrational properties on lattice thermal conductivity. In our case, we are interested in the vibrational contribution to phase stability, and we calculate phonons using the supercell frozen phonon method (as implemented in the program described in ref 34). The vibrational entropy of formation with respect to the pure constituents can be expressed $\Delta S_{vib}(\sigma) = S_{vib}(\sigma) - (1-x)S_{vib}^{A} - xS_{vib}^{B}$, where $S_{vib}^{A}$, $S_{vib}^{B}$, and $S_{vib}(\sigma)$ are vibrational entropies of pure constituents A, B, and the mixed compound $\sigma$ with composition $x$. Our calculations of the vibrational entropy of $SrPb_3S_4$, $SrPbS_2$, and $Sr_3PbS_4$ with respect to pure constituent PbS and SrS show small negative formation vibrational entropies as listed in Table S2 in the Supporting Information. At high temperatures, the negative $\Delta S_{vib}(\sigma)$ will partially cancel the negative formation enthalpy in the free energy $\Delta G = \Delta H - T\Delta S$, indicating a competition for the stability of the ordered phases. However, the magnitude of $\Delta S_{vib}$ is small, and thus this effect should be minor.

**3.3. Electronic Structure and Strain Energy Analysis.** We further probed the difference between the phase stability of the PbS−CaS and PbS−SrS systems in terms of both electronic structure and strain energies. We thus investigated the electronic density of states of $SrPbS_2$ and $CaPbS_2$ in $L1_0$ structure. Note that the $CaPbS_2$ is not a stable compound as indicated in Figure 1a, but a hypothetical compound in the same structure as $SrPbS_2$. For the ordered phases $SrPb_3S_4$, $SrPbS_2$, and $Sr_3PbS_4$, the band structures and density of states are also shown in Supporting Information Figure S2. Clearly, all three phases possess direct band gaps.

There is a significant difference between the PbS−CaS and PbS−SrS systems in terms of lattice strain: the lattice constant difference between PbS and CaS (4% mismatch) is much larger than that of PbS and SrS (1% mismatch). To quantitatively evaluate the lattice mismatch effects on the mixing formation energy, we have calculated the coherency strain energy.[35] In a coherent two-phase mixture, the system maintains some degree of coherency, or lattice registry, between the two phases. The coherently constrained phases share the same lattice constant in the plane of the interface between two constituents, leading to a coherent strain energy. This strain energy is the penalty required to deform two phases to the same lattice parameter along a crystallographic plane (but relaxed perpendicular to this plane). The strain energy to maintain coherency at an interface between two phases is necessarily dependent on the orientation of the interface. The details of coherency strain energy calculations have been presented elsewhere.[8,36] For both PbS−CaS and PbS−SrS mixing systems, we consider three directions of [100], [110], and [111] at a full range of second phase content to examine coherency strain energies. As can be seen from Supporting Information Figure S3, the coherent strain energies in the CaS system are much larger than those in the SrS system, due to the larger lattice mismatch. For the PbS−CaS system, the strain energies range from about 26 to 46 meV/cation at 50% mixing, which are comparable to the formation energies (Figure 1), indicating that lattice mismatch and strain play the dominant role in the phase-separating behavior. This decisive role of strain energy is consistent with


dx.doi.org/10.1021/ja411857y | J. Am. Chem. Soc. 2014, 136, 1628−1635

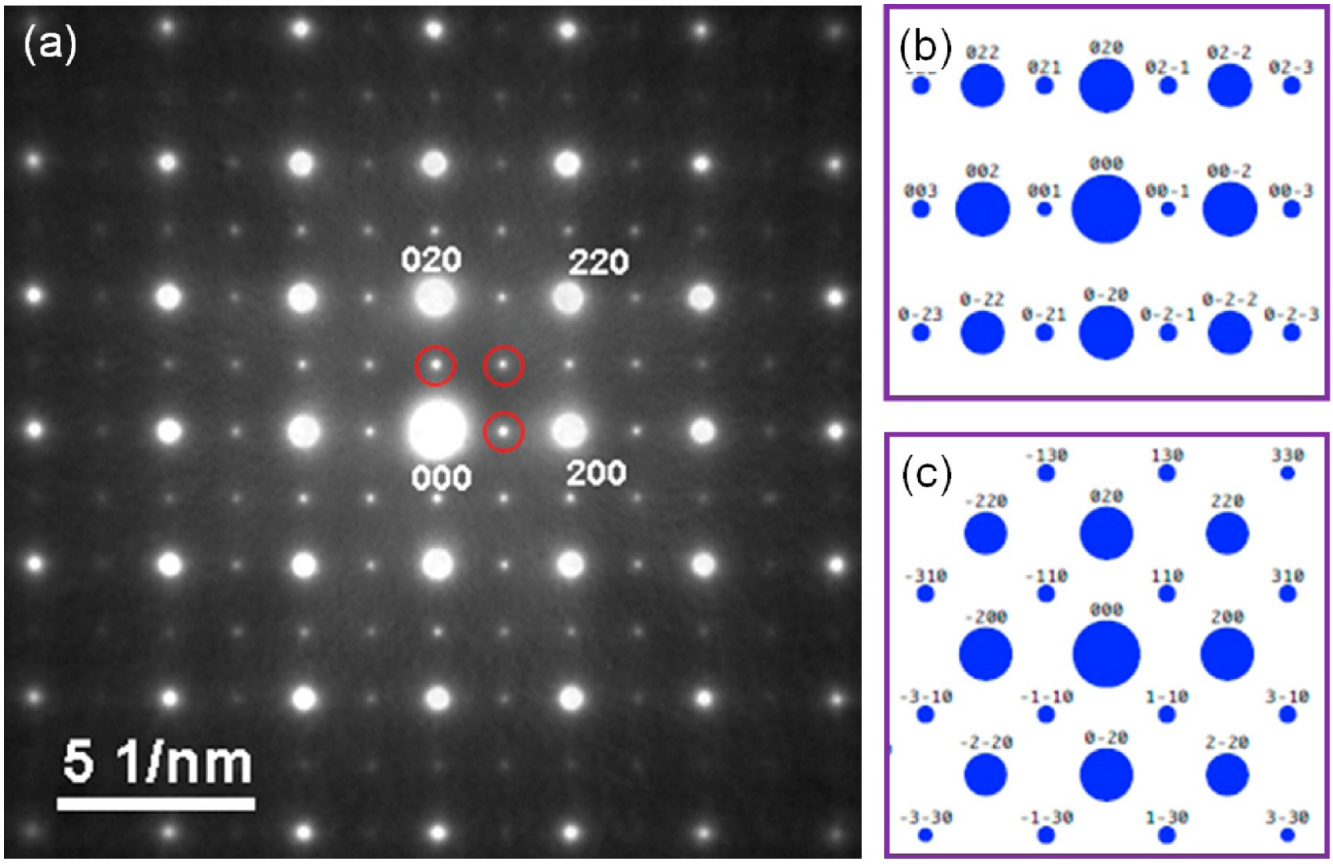


**Figure 3.** (a) [001] zone SADP of $SrPbS_2$ showing superlattice reflections arising from $L1_0$ ordering, and (b,c) simulated diffraction pattern of $L1_0$ ordered structure with *a* and *c* zone axes, respectively. Note that the experimental diffraction pattern contains all three variants, that is, [100], [010], and [110], of the ordered phase (circled in red), corresponding to three orthogonal symmetry-equivalent crystallographic variants with *c* axis parallel to the *a*, *b*, and *c* axes of the original rock salt structure.

the long-standing paradigm of phase separation in these isovalent semiconductor alloys. However, for PbS−SrS, the lattice mismatch, and hence the coherency strain energy, is very small (only ∼1 meV/cation). Hence, strain energy does not control the phase stability of this system, providing the explanation for the unusual emergence of ordered phases in PbS−SrS.

We can also ascertain the role of coherency strain on the calculated phase diagrams. By subtracting the coherency strain energy from the incoherent mixing enthalpy, we obtain the "coherent mixing enthalpy". Positive or negative values of coherent mixing enthalpy will determine whether the coherent phase diagram is phase separating or compound forming. In the PbS−CaS system, the lowest coherent strain energies shown in Supporting Information Figure S3a are not large enough to make the coherent mixing energy (shown in Figure 1a) negative, and hence the coherent phase diagram should still show a miscibility gap, albeit at depressed temperatures. For the PbS−SrS system, the coherency strain energies are very small and only play a minor role in the incoherent mixing enthalpy, and hence the phase diagram.

**3.4. XRD and TEM Observations.** To experimentally investigate the unexpected prediction of ordered compounds, in PbS−SrS, we have synthesized a series of compositions $Sr_xPb_{1-x}S$ ($x$ = 0, 0.10, 0.25, 0.50, 0.75, 0.90, and 1.0). Supporting Information Figure S4 shows the XRD patterns for these compositions. We find, in qualitative contrast to the PbS−CaS measurements, all compositions in PbS−SrS show a single phase with rocksalt structures. These patterns are consistent with the existence of single phase solid solutions at elevated temperatures indicated in the calculated phase diagram. To verify the existence of ordering on the rocksalt structure is more subtle, and hence we employ transmission electron microscopy and electron diffraction to investigate the ordering/disordering and phase-separation processes in the $Sr_xPb_{1-x}S$ system. The local structure of a slow-cooled sample (from 1423 to 300 K in 8 h) with a nominal composition corresponding to $SrPbS_2$ was analyzed by HRTEM imaging and electron diffraction. A selected-area diffraction pattern (SADP) taken from the $SrPbS_2$ specimen along the [001] zone axis is shown in Figure 3. Apart from the primary diffraction spots, for example, the {200}, {020}, and {220} reflections, addition sets of weak spots (circled in red) at the {100}, {010}, and {110} positions can also be clearly seen. The presence of these additions spots, which are kinematically forbidden in the disordered rock-salt structure, is a clear evidence of atomic ordering along these directions. These superlattice reflections are consistent with the simulated diffraction patterns (Figure 3b and c) of the ordered $SrPbS_2$ possessing an $L1_0$ cation ordering with alternating layers of Pb and Sr in a tetragonal structure. However, one should not expect the simultaneous appearance of the {100}, {010}, and {110} reflections for an ordered $L1_0$ structure when observing along either ⟨*a*⟩, ⟨*b*⟩, or ⟨*c*⟩ direction. According to the simulation, the {100}, {010}, and {110}-type superlattice reflections arise, respectively, from the *a*, *b*, and *c* variants (i.e., the $L1_0$ *z* axis parallel to the −*a*, *b*, and *c* directions


dx.doi.org/10.1021/ja411857y | J. Am. Chem. Soc. 2014, 136, 1628−1635

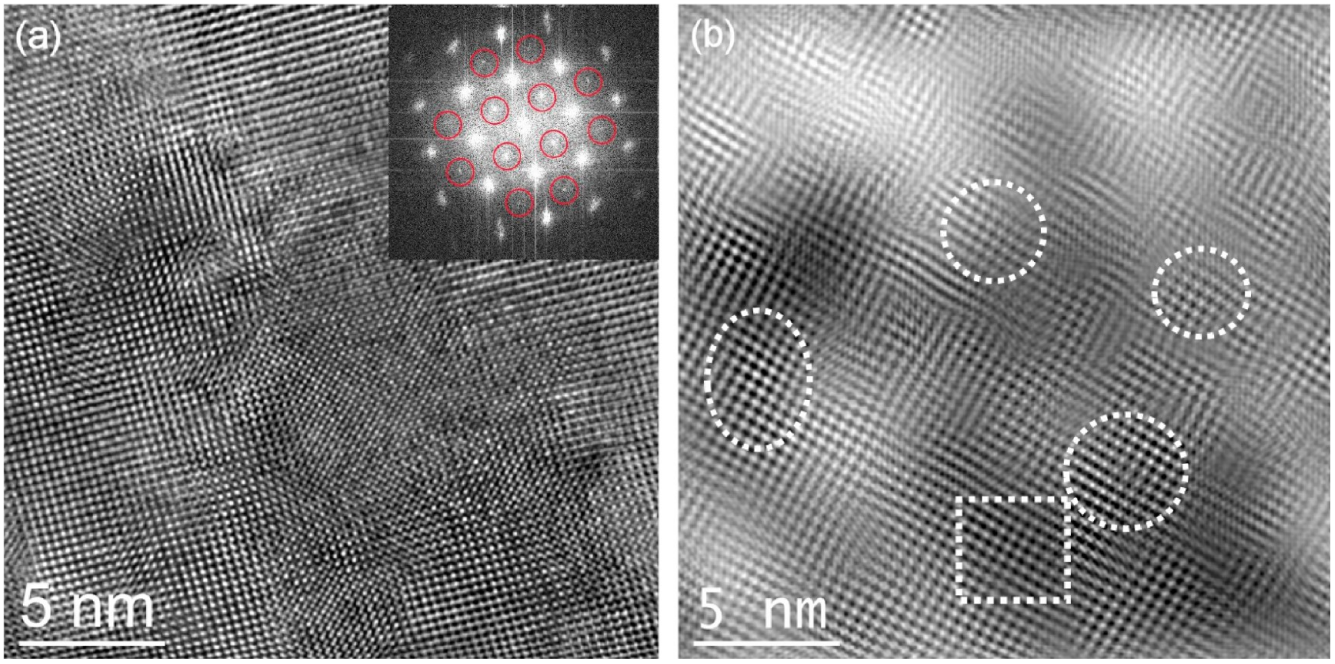


**Figure 4.** (a) High-resolution atomic observation along the [001] zone axis of the ordered $SrPbS_2$. The FFT inset showing {110} type superlattice reflections (circled in red), which is consistent with the simulated diffraction pattern in Figure 3(c) indicating the *c*-variant of the $L1_0$ ordering in this local area. (b) Inverse FFT image obtained by using exclusively the superlattice reflections showing domain-like mosaic microstructure (examples circled in dotted lines) resulting from the ordering.

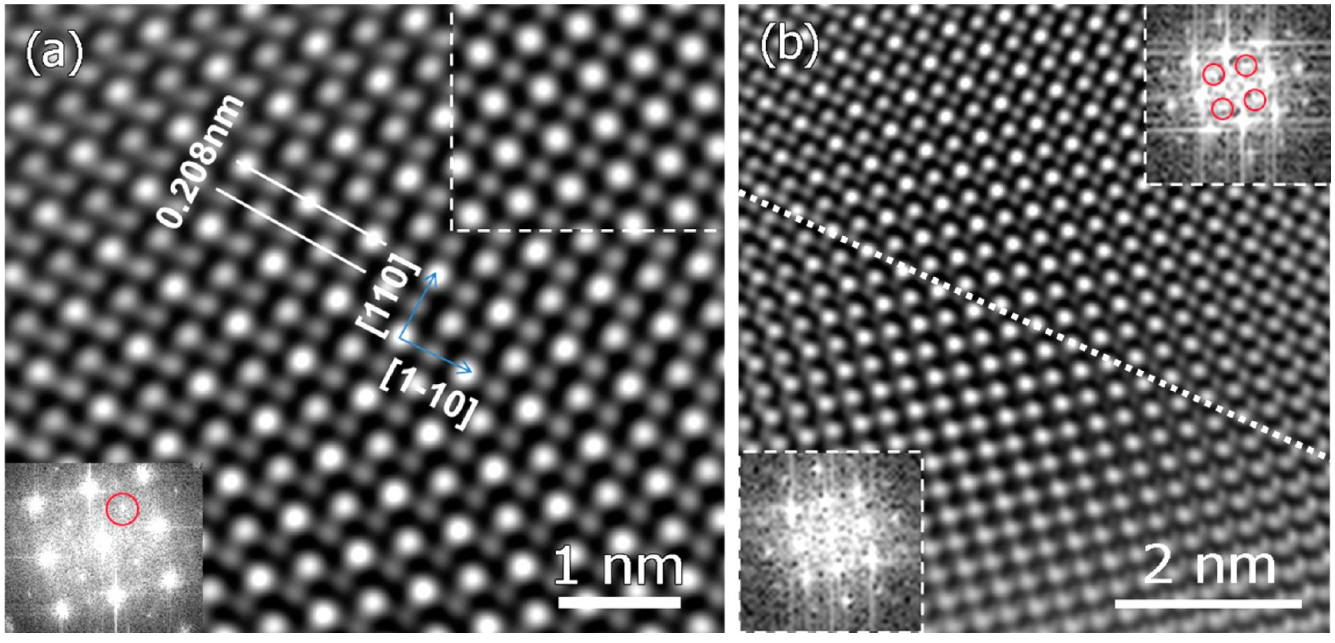


**Figure 5.** (a) A high-resolution image taken from the framed area in Figure 4a for $SrPbS_2$, which shows clearly the atomic structure of the *c*-variant $L1_0$ ordered phase implied by the {110} type superlattic reflections in the lower-left FFT inset (circled), the top-right inset being the simulated HREM image of the *c* variant of the $L1_0$ structured $SrPbS_2$, which is consistent with the experimental image. (b) A lower magnification view of (a), showing the area containing both ordered (top right) and disordered (lower left) domains (approximately separated by the dashed line), which are indicated by the presence and absence of superlattice reflections (see the corresponding inset FFTs), respectively.

of the original cubic structure, respectively). Therefore, the diffraction pattern in Figure 3 clearly indicates the coexistence of all three symmetry equivalent variants in the selected area used to acquire the diffraction pattern. As the reflection intensity of the three variants appears close to each other, it implies (to a good approximation) that these variants are energetically degenerate with equal probability for ordering to occur along the *a*, *b*, and *c* directions. The atomic ordering and the coexistence of the *a*, *b*, and *c* variants are further confirmed by the observation of the superlattice reflections along the [111] zone axis of the specimen; see Supporting Information Figure S5. Because these three orthogonal variants are energetically equivalent, it is not unusual to form domain-like mosaic microstructure of the ordered phase where there is an


dx.doi.org/10.1021/ja411857y | *J. Am. Chem. Soc.* 2014, 136, 1628−1635

equal probability for each of the variants to exist in a given microstructure. The size of these domains ranges typically from ~5 to 15 nm, as shown by the dark field image in Supporting Information Figure S6(a).

A high-resolution phase contrast image of $SrPbS_2$, Figure 4, was taken from a region corresponding to the diffraction pattern shown in Figure 3, with the fast Fourier transformation (FFT) of the HREM shown as the inset. Different from the case of Figure 3a where three symmetry-equivalent variant domains of the tetragonal $L1_0$ structure coexist with their *c* axes mutually oriented perpendicularly, the FFT clearly shows the presence of only the [110]-type super reflections, whereas the [001]-type super reflections were absent, indicating a single-variant *c*-domain nature of this local area (*c*-axes oriented normal to the film plane). An inverse FFT image obtained by using only the {110}-type superlattice refletions is shown as Figure 4b, which confirms the domain-like mosaic microstructure of the ordered $L1_0$ phase. A close-up high-resolution image of the ordered $L1_0$ phase is shown in Figure 5a, with a simulated image of the $L1_0$ structured $SrPbS_2$ shown as an inset, which is consistent with the HREM image, as further confirmation of the existence and the *c*-variant nature of the $L1_0$ ordering in this domain. Figure 5b, which is a lower magnification view of Figure 5a, however, contains both ordered and disordered domains, as is indicated in the image. In the ordered domains, extra spots corresponding to the {110}-type superlattice reflections can be clearly seen, which are absent in the disordered region. Measurement of the {110} superlattice reflections gives the {110} plane spacing of ~0.416 nm, which is close to the 0.415 nm of the theoretical value. In Figure 5a, the {220} atomic planes of the ordered phase with spacing of ~0.208 nm can also be clearly resolved as indicated in the image.

We also attempted to assess the tetragonality of the ordered $SrPbS_2$ phase. The existence of {001} and {110} superlattice reflections at the half distance of the (200), (020), and (220), respectively, is a clear indicatoin that the *c*/*a* ratio (*c* is the lattice parameter in the *z* direction, and *a* is the lattice parameter in the *x* or *y* direction) is close to unity, consistent with small tetragonality of 1.001 obtained by our DFT calculations. With such a low tetragonality, a cubic (rocksalt)-to-tetragonal ($L1_0$) transformation of the $SrPbS_2$ will likely lead to a very small strain energy, without producing much difficulty for accommodating stress relaxation. As a result, this system is amenable to ordering that can be readily achieved under proper (mild) conditions such as slow cooling from the melting temperature or low temperature annealing. TEM studies on a super slowly cooled specimen (573 to 300 K in 2 weeks) showed that the intensity of superlattice reflections increased dramatically (not shown), consistent with increasing of atomic ordering under slow cooling or annealing conditions. Thus, combined electron diffraction and high-resolution phase contrast imaging unequivocally confirm the theoeretical prediction of disorder−order transition in $SrPbS_2$. Our results are thus qualitatively different from those of previous calculations on $Pb_{1-x}Sr_xS$, where the phase diagram is predicted to contain a miscibility gap.[37] This is possibly because their mixing energies are simply calculated by a regular-solution model without a full exploration of the configurational ternary phase space, as we have done in the present work.

**3.5. Band Gap Measurements.** Armed with the discovery of these new single phases of $Sr_xPb_{1-x}S$, we carried out electronic band gap measurements and calculations to further clarify the properties of these materials. As shown in Figure 6a, the band gaps increase with increasing SrS fraction. Relative to

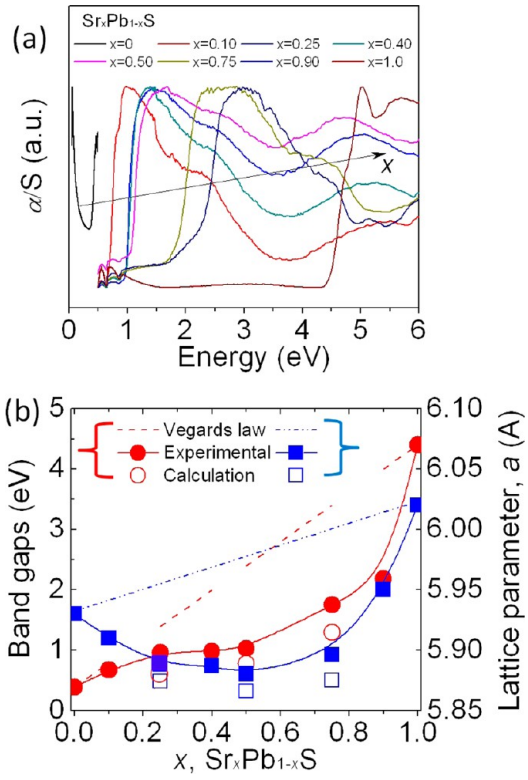


**Figure 6.** (a) Band gaps for the experimental $Sr_xPb_{1-x}S$ phases and (b) the band gaps and lattice parameters as a function of SrS content; the dashed line corresponds to the Vegards law for $Sr_xPb_{1-x}S$ solid solutions. "●" ("■") are experimental data for band gap (lattice parameter), while "○" ("□") is calculation for band gap (lattice parameter).

a simple linear behavior with composition (dashed line), the observed band gaps exhibit a strong bowing, which are consistent with the calculations for the corresponding ordered phases as shown in Figure 6b. This agreement between calculated and observed gaps is indirect evidence that these phases are ordered (i.e., they are compounds) rather than solid solutions. To further corroborate this, we also calculated band gaps of hypothetical solid solutions from SQS structures for the three compositions $SrPb_3S_4$, $SrPbS_2$, and $Sr_3PbS_4$. The calculated SQS band gaps are 1.35, 2.02, and 2.71 eV, respectively, which are significantly different from those of the ordered phases (0.68, 1.02, and 1.41 eV, respectively) and the observed gaps. Thus, these calculations again point to the fact that these phases are ordered compounds, rather than disordered solid solutions. As shown in Figure 6b, the measured lattice parameters are also very close to the calculated values, with both showing a negative deviation from Vegard's Law for the ordered compound lattice parameters.

## 4. SUMMARY AND CONCLUSIONS

We presented an example of effective discovery of new materials by a combination of DFT-based methods with experimental synthesis and characterization techniques. Analogous to most other ternary III−V or IV−VI semiconductor alloys, we find that bulk phase separation is thermodynamically preferred for PbS−CaS. However, we predict the existence of


dx.doi.org/10.1021/ja411857y | J. Am. Chem. Soc. 2014, 136, 1628−1635

stable, ordered ternary compounds in the PbS−SrS system. These phases are previously unreported ordered rocksalt-based compounds: $SrPb_3S_4$, $SrPbS_2$, and $Sr_3PbS_4$. Experimental confirmation of these ordered compounds in $Sr_xPb_{1-x}S$ (but not $Ca_xPb_{1-x}S$) illustrates the effectiveness of the combined computational-experimental approach for identification of new, stable materials. The direct band gaps of these new materials point to potential applications as solar energy conversion and optoelectronic materials. This study also provides a general approach for future studies of complex phase relations in multicomponent chalcogenide systems.

## ■ ASSOCIATED CONTENT

### Supporting Information

XRD patterns for the nominal composition of $CaPbS_2$, CaS, and PbS (Figure S1); band structures of $SrPb_3S_4$, $SrPbS_2$, and $Sr_3PbS_4$ (Figure S2); comparison of coherent strain energies between PbS−CaS and PbS−SrS (Figure S3); XRD patterns for the experimental $Sr_xPb_{1-x}S$ phases (Figure S4); an experimental SADP along [111] zone axis for the $SrPbS_2$ phase and corresponding diffraction pattern from simulation (Figure S5); TEM dark field (DF) imaging highlighting the ordered domains of $SrPbS_2$ with a size range of about 5−15 nm, and a close-up image (Figure S6); band gaps for the experimental $SrPbS_2$ phase and the 50% PbS + 50% SrS mixture, which shows the separate band gaps corresponding to PbS and SrS, respectively (Figure S7); the parameters of clusters and effective cluster interactions for PbS/CaS and PbS/SrS systems (Table S1); and lattice constants and DFT calculated formation vibrational entropy at 400 K (Table S2). This material is available free of charge via the Internet at http://pubs.acs.org.

## ■ AUTHOR INFORMATION


### Corresponding Author

c-wolverton@northwestern.edu

### Author Contributions

[§]These authors contributed equally.


### Notes

The authors declare no competing financial interest.

## ■ ACKNOWLEDGMENTS

This contribution is based upon work supported as part of the Revolutionary Materials for Solid State Energy Conversion, an Energy Frontier Research Center funded by the U.S. Department of Energy, Office of Science, Office of Basic Energy Sciences under Award Number DE-SC00010543. Access to facilities of the NU*ANCE* Center and high performance computational resources at Northwestern University is acknowledged.

## ■ REFERENCES


(1) Zunger, A.; Mahajan, S. *Handbook on Semiconductors*; North-Holland: Amsterdam, 1992; Vol. *3b*.

(2) Stringfellow, G. B. *J. Cryst. Growth* **1974**, *27*, 21.

(3) Dandrea, R. G.; Bernard, J. E.; Wei, S. H.; Zunger, A. *Phys. Rev. Lett.* **1990**, *64*, 36.

(4) Moon, C.-Y.; Wei, S.-H.; Zhu, Y. Z.; Chen, G. D. *Phys. Rev. B* **2006**, *74*, 233202.

(5) Fan, X. F.; Shen, Z. X.; Lu, Y. M.; Kuo, J.-L. *New J. Phys.* **2009**, *11*, 093008.

(6) Liu, J. Z.; Zunger, A. *Phys. Rev. B* **2008**, *77*, 205201.

(7) Mbaye, A. A.; Wood, D. M.; Zunger, A. *Phys. Rev. B* **1988**, *37*, 3008.

(8) Doak, J. W.; Wolverton, C. *Phys. Rev. B* **2012**, *86*, 144202.

(9) Gomyo, A.; Makita, K.; Hino, I.; Suzuki, T. *Phys. Rev. Lett.* **1994**, *72*, 673.

(10) Zhao, L. D.; Lo, S. H.; He, J. Q.; Li, H.; Biswas, K.; Androulakis, J.; Wu, C. I.; Hogan, T. P.; Chung, D. Y.; Dravid, V. P.; Kanatzidis, M. G. *J. Am. Chem. Soc.* **2011**, *133*, 20476.

(11) Zhao, L. D.; He, J. Q.; Hao, S.; Wu, C. I.; Hogan, T. P.; Wolverton, C.; Dravid, V. P.; Kanatzidis, M. G. *J. Am. Chem. Soc.* **2012**, *134*, 16327.

(12) Biswas, K.; He, J. Q.; Zhang, Q. C.; Wang, G. Y.; Uher, C.; Dravid, V. P.; Kanatzidis, M. G. *Nat. Chem.* **2011**, *3*, 160.

(13) Biswas, K.; He, J. Q.; Blum, I. D.; Chun, I. W.; Hogan, T. P.; Seidman, D. N.; Dravid, V. P.; Kanatzidis, M. G. *Nature* **2012**, *490*, 414.

(14) Abraham, N. L.; Probert, M. I. J. *Phys. Rev. B* **2006**, *73*, 224104.

(15) Pickard, C. J.; Needs, R. J. *J. Phys.: Condens. Matter* **2011**, *23*, 053201.

(16) Glass, C. W.; Oganov, A. R.; Hansen, N. *Comput. Phys. Commun.* **2006**, *175*, 713.

(17) Zakutayev, A.; Zhang, X.; Nagaraja, A.; Yu, L.; Lany, S.; Mason, T. O.; Ginley, D. S.; Zunger, A. *J. Am. Chem. Soc.* **2013**, *135*, 10048.

(18) Curtarolo, S.; Hart, G. L. W.; Nardelli, M. B.; Mingo, N.; Sanvito, S.; Levy, O. *Nat. Mater.* **2013**, *12*, 191.

(19) Ceder, G.; Chiang, Y.-M.; Sadoway, D. R.; Aydinol, M. K.; Jang, Y.-I.; Huang, B. *Nature* **1998**, *392*, 694.

(20) Ceperley, D. M.; Alder, B. J. *Phys. Rev. Lett.* **1980**, *45*, 566.

(21) Perdew, J. P.; Chevary, J. A.; Vosko, S. H.; Jackson, K. A.; Pederson, M. R.; Singh, D. J.; Fiolhais, C. *Phys. Rev. B* **1992**, *46*, 6671.

(22) Kresse, G.; Furthmuller, J. *Phys. Rev. B* **1996**, *54*, 11169.

(23) Sanchez, J. M.; Ducastelle, F.; Gratias, G. *Physica A* **1984**, *128*, 334.

(24) van de Walle, A.; Asta, M.; Ceder, G. *CALPHAD J.* **2002**, *26*, 539.

(25) van de Walle, A.; Asta, M. *Modell. Simul. Mater. Sci. Eng.* **2002**, *10*, 521.

(26) Li, H.; Malliakas, C. D.; Liu, Z.; Peters, J. A.; Jin, H.; Morris, C. D.; Zhao, L.; Wessels, B. W.; Freeman, A. J.; Kanatzidis, M. G. *Chem. Mater.* **2012**, *24*, 4434.

(27) (a) Kortum, G. F. A. *Reflectance Spectroscopy: Principles, Methods, Applications*; Springer: New York, 1969. (b) Chondroudis, K.; McCarthy, T. J.; Kanatzidis, M. G. *Inorg. Chem.* **1996**, *35*, 840. (c) McCarthy, T. J.; Tanzer, T. A.; Kanatzidis, M. G. *J. Am. Chem. Soc.* **1995**, *117*, 1294.

(28) Zunger, A.; Wei, S. H.; Ferreira, L. G.; Bernard, J. E. *Phys. Rev. Lett.* **1990**, *65*, 353.

(29) Klemm, W. *Angew. Chem.* **1950**, *62*, 133.

(30) Ozolins, V.; Wolverton, C.; Zunger, A. *Phys. Rev. B* **1998**, *58*, R5897.

(31) Zhang, Y.; Skoug, E.; Cain, J.; Ozoliņs, V.; Morelli, D.; Wolverton, C. *Phys. Rev. B* **2012**, *85*, 054306.

(32) Nielsen, M. D.; Ozolins, V.; Heremans, J. P. *Energy Environ. Sci.* **2013**, *6*, 570.

(33) Shiomi, J.; Esfarjani, K.; Chen, G. *Phys. Rev. B* **2011**, *84*, 104302.

(34) Wolverton, C.; Ozolins, V. *Phys. Rev. B* **2007**, *75*, 64101.

(35) Khachatury, A. G. *Coherent Phase Transformations in High Performance Materials*; Wiley Blackwell: New York, 2008.

(36) Wolverton, C.; Ozolins, V.; Zunger, A. *J. Phys.: Condens. Matter* **2000**, *12*, 2749.

(37) Labidi, S.; Labidi, M.; Meradji, H.; Ghemid, S.; El Haj Hassan, F. *Comput. Mater. Sci.* **2011**, *50*, 1077.